Electronic Supplemental Information

Study of defect Induced magnetic anisotropy in MWCNT and RGO dispersed SnTe using spin resonance and magnetic measurement

Subhadip Ghosh†, Shivam Shukla and Sanjeev Kumar Srivastava‡
†School of Nano Science and Technology Indian Institute of Technology, Kharagpur, 721302
‡Department of Physics, Indian Institute of Technology, Kharagpur, 721302

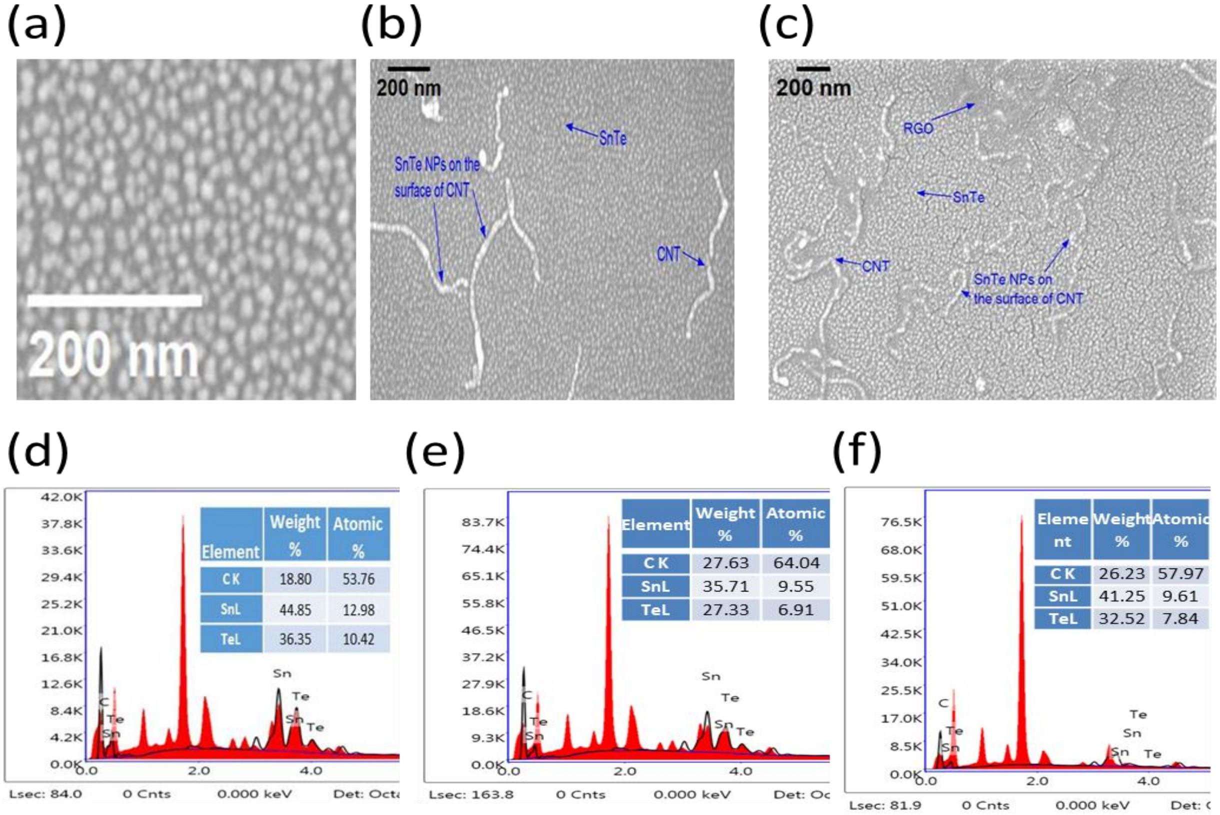

(d)

Element	Weight %	Atomic %
C K	18.80	53.76
SnL	44.85	12.98
TeL	36.35	10.42

(e)

Element	Weight %	Atomic %
C K	27.63	64.04
SnL	35.71	9.55
TeL	27.33	6.91

(f)

Element	Weight %	Atomic %
C K	26.23	57.97
SnL	41.25	9.61
TeL	32.52	7.84

FIG. S1 FESEM image of (a) SnTe, (b) CTS, and (c) SRC. EDX spectra of (d) SnTe, (e) CTS, and (f) SRC.

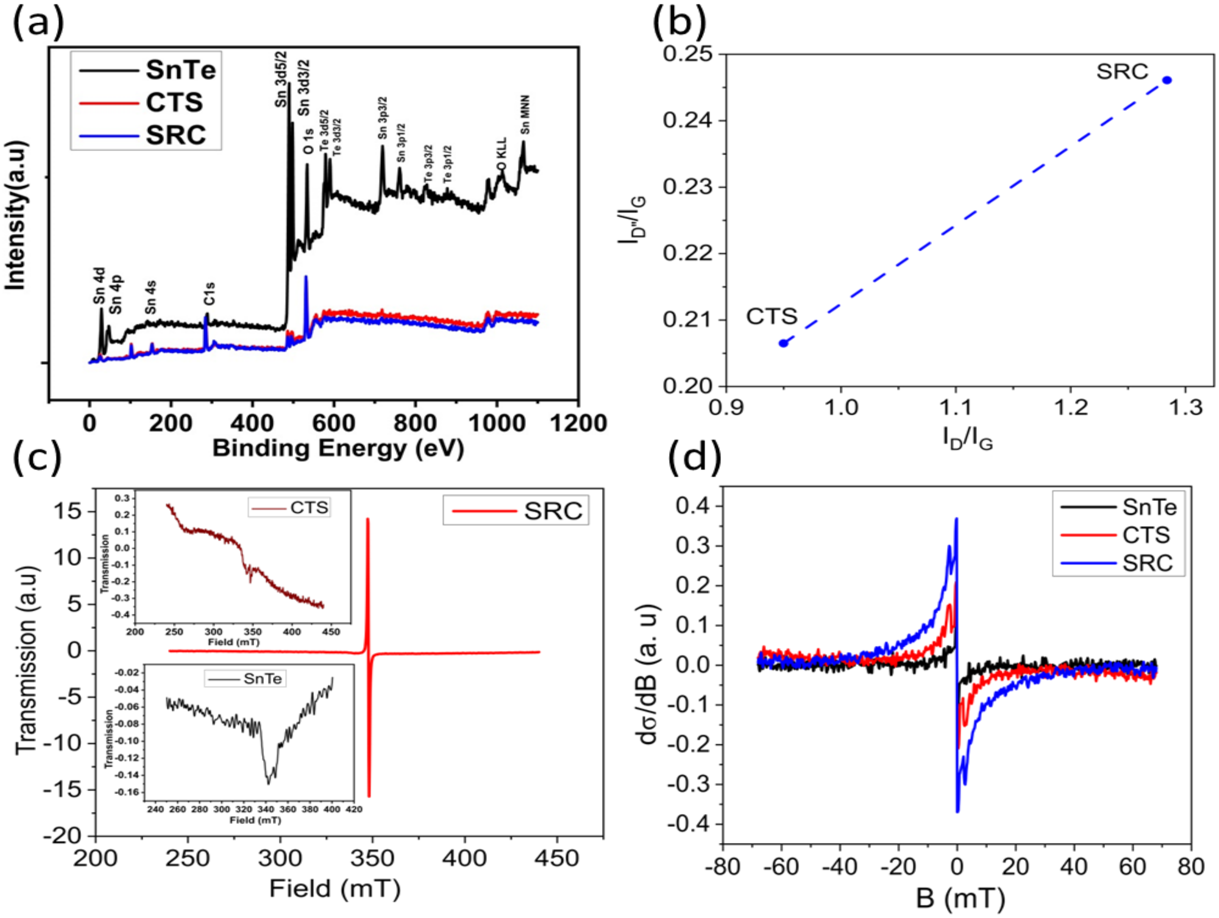

FIG. S2 (a) XPS survey spectra of SnTe, CTS, and SRC (b) The variation of intensity of $I_{D''}/I_G$ to I_D/I_G of CTS and SRC from Raman spectra, (c) Comparison of low-temperature (12K) ESR spectra of SnTe, CTS, and SRC, (d) Comparison of Low temperature (12 K) ESR differential conductivity of SnTe, CTS, and SRC.

TABLE S I XPS Sn oxidation peaks of SnTe, CTS, and SRC.

Sample Name	$Sn^{+2}_{3d5/2}$	$Sn^{+2}_{3d3/2}$	$Sn^{+4}_{3d5/2}$	$Sn^{+4}_{3d3/2}$	$Sn^{sat}_{3d5/2}$	$Sn^{sat}_{3d3/2}$
SnTe	485.84	494.2	487.02	495.31	-	-
CTS	486.01	494.3	486.84	494.86	488.52 and 489.53	496.64 and 497.86
SRC	485.95	494.27	486.93	494.96	488.20 and 489.13	495.91 and 497.5

TABLE S II XPS Te oxidation peaks of SnTe, CTS, and SRC.

Sample Name	$Te^{-2}_{3d5/2}$	$Te^{-2}_{3d3/2}$	$Te^{+4}_{3d5/2}$	$Te^{+4}_{3d3/2}$	$Te^{sat}_{3d5/2}$	$Te^{sat}_{3d3/2}$
SnTe	571.75	582.13	576.13	586.58	-	-
CTS	571.99	582.33	576.17	586.44	579.07	587.84 and 589.55
SRC	572.13	582.74	576.40	586.75	578.87	587.84 and 589.55

TABLE S III XPS C 1s oxidation peaks of CTS and SRC.

Sample Name	$C{=}C_{1s}$	$C\text{-}C_{1s}$, $C\text{-}Sn_{1s}$	$C\text{-}Te_{1s}$	$C{=}O_{1s}$, $\text{-}O\text{-}CO_{1s}$
CTS	284.54	285.45	286.57	288.13
SRC	244.61	285.24	286.06	287.28

TABLE S IV XPS O 1s oxidation peaks of CTS and SRC.

Sample Name	$C{=}O_{1s}$	$C\text{-}O_{1s}$	$C\text{-}OH_{1s}$
CTS	530.46	532.06	534.017
SRC	530.68	532.08	533.74

TABLE S V The approximate percentage of Sn, Te, and C atoms in bare and MWCNT, RGO-anchored SnTe nano grains.

Name of the composite	Symbol of present element	Raw XPS peak area from fitting (I)	Relative Sensitivity Factor (RSF) (S)	Normalized area by RSF (I/S)	Total corrected intensity (Σ I/S)	Atomic percentage (I/S)/Σ (I/S)*100	Atomic percentage Without C
SnTe	Sn	39915.04	4.09	9759.18		44.88	51.92
	Te	44275.12	4.9	9035.74	18794.92	41.56	48.08
	C	6435.75	0.296	2947.5	21742.42	13.55	
CTS	Sn	13520.51	4.09	3305.75		42.43	51.41
	Te	15311.117	4.9	3124.73	6430.48	40.11	48.59
	C	402.68	0.296	1360.41	7790.89	17.46	
SRC	Sn	10122.42	4.09	2474.92		42.48	52.6
	Te	10925.598	4.9	2229.714	4704.634	38.27	47.4
	C	331.99	0.296	1121.59	5826.22	19.25	

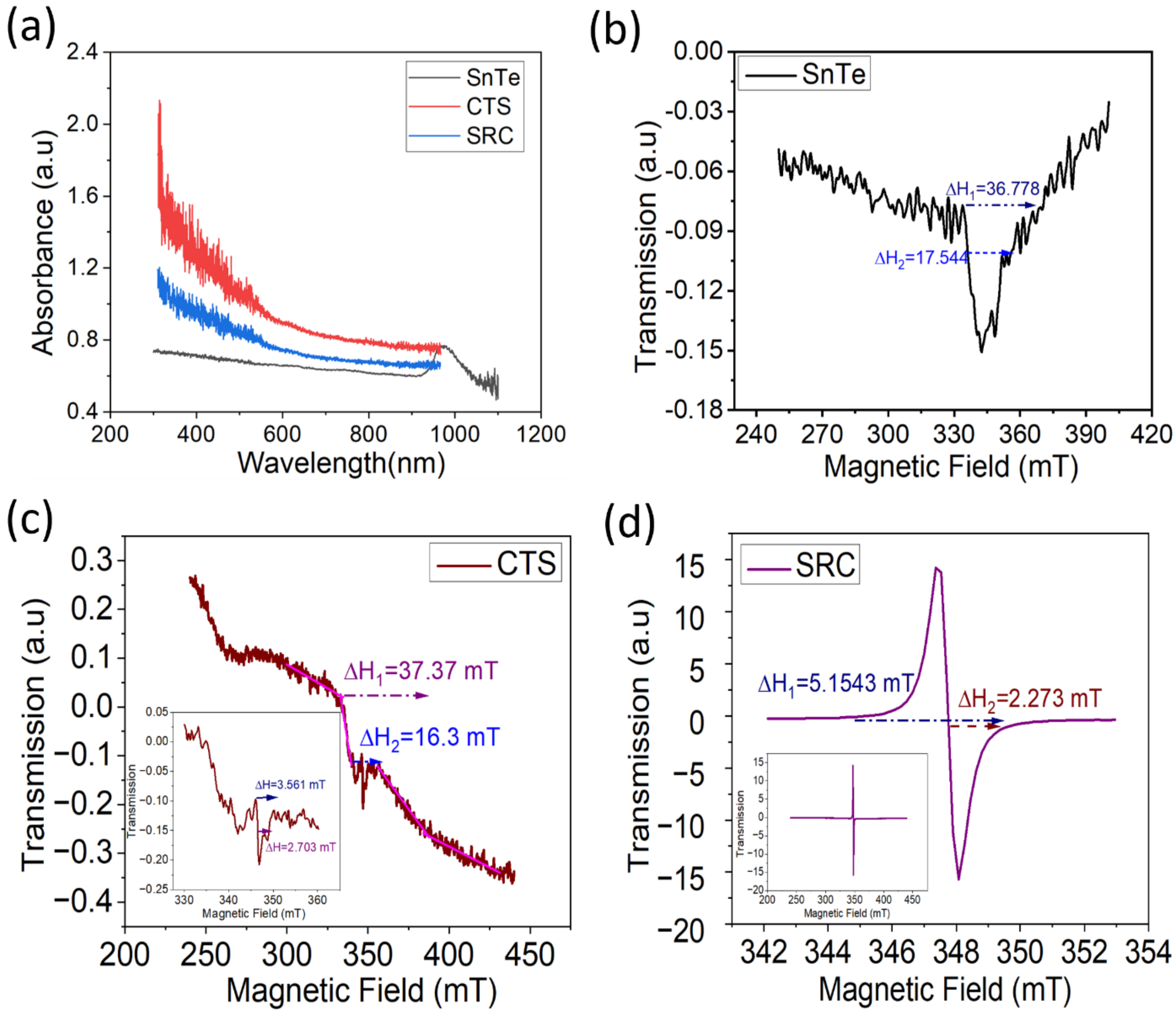

FIG. S3 (a) UV-VIS absorption spectra of SnTe, CTS, and SRC. ESR magnetic resonance spectra of (b) SnTe, (c) CTS (inset shows 2nd magnetic resonance close to resonance field), and (d) SRC.

Estimation of atomic percentage from XPS peak area ratio:

To further verify the atomic composition obtained from EDX, we calculated the atomic percentages of Sn, Te, and C using the XPS peak area ratios. Table S V presents the estimated atomic percentages of Sn, Te, and C in both bare SnTe and in SnTe nano-grains anchored with MWCNT (multi-wall carbon nanotubes) and RGO (reduced graphene oxide).

By comparing the atomic percentages with and without carbon, we estimated the carbon content introduced by MWCNT and RGO in the CTS and SRC samples. The contribution of carbon from MWCNT in CTS is approximately 3.91% (17.46% – 13.55%), while the combined contribution from MWCNT and RGO in SRC is approximately 5.7% (19.25% – 13.55%).

Approximate semi-quantitative trends of carrier dynamics from PL and UV-VIS studies:

Based on steady-state PL and UV-VIS absorbance measurements (Figure S3 (a)), we can approximately estimate semi-quantitative trends in carrier dynamics. The total recombination lifetime (τ) is governed by both radiative and non-radiative processes, and can be expressed[3] as:

$$1/\tau = 1/\tau_r + 1/\tau_{nr} \qquad \text{........ (1)}$$

Steady-state carrier density (n) can be estimated from τ and carrier generation rate (G) via the relation

$$n=G\tau \qquad \text{......... (2)}$$

We can estimate G as

$$G = \frac{\alpha Pexc}{h\nu A} \qquad \text{.......... (3)}$$

Where α is the absorption coefficient, P_{exc} is the excitation power, hν is the photon energy, and A is the excitation area.

Under continuous excitation, PL intensity is proportional to the radiative recombination rate

$$I_{PL} \propto \eta G \ \propto \tau/(\tau_r + \tau_{nr}) .G \qquad \text{............ (4)}$$

Where η is the quantum efficiency.

The average PL intensity of bare SnTe is approximately seven times higher than that of CTS and SRC, indicating a longer effective carrier lifetime and slower recombination in bare SnTe nanograins. Incorporating MWCNT and RGO into SnTe reduces the PL intensity and broadens the FWHM of the PL peaks. This suggests a decrease in Sn vacancy concentration and enhanced non-radiative recombination due to the higher carrier density in MWCNT and RGO, which passivates radiative PL emission. The observed blue and red shifts in the PL peaks upon incorporation of MWCNT and RGO reflect changes in defect and impurity states within SnTe. From the UV-VIS-NIR absorption spectrum (Figure S3 (a)), the absorption coefficient (α) is estimated using the relation:

$$\alpha = \frac{2.303A}{d} \qquad \text{............. (5)}$$

where A is the absorbance and d is the sample thickness.

A 20x objective lens was used along with a 20 mW laser operating at an excitation wavelength of 532 nm. The intensity of the incident photons is calculated using the following relation:

$$I_{photon} = P_{exc}/(h\nu.A_{spot}) \qquad \text{............... (6)}$$

From the above equation, the calculated photon intensity at 532 nm is 2.7271×10^{23} photons/cm^2. For the calculation of n, we assume the value of τ in the order of 1 ns. Accurate estimation of the recombination lifetime (τ) requires time-resolved PL, transient absorption, or pump-probe spectroscopy measurements. However, due to the unavailability of these facilities at present, we are unable to perform such measurements. Table S VI describes the approximate variation of α, G, and n of SnTe, CTS, and SRC.

TABLE S VI Approximate variation of α, G, and n of SnTe, CTS, and SRC.

Sample Name	α	G (carrier/cm^3)	n (/cm^3)
SnTe	0.810445	2.21x10^{23}	2.21x10^{14}
CTS	1.031	2.81x10^{23}	2.81x10^{14}
SRC	0.444702	1.219x10^{23}	1.219x10^{14}

The photogeneration rate (G) for SnTe, CTS, and SRC follows the ratio: $G_{SnTe} : G_{CTS} : G_{SRC} = 1.813 : 2.305 : 1$.

The ratio of the integrated PL intensity (area under the PL spectra) for SnTe, CTS, and SRC is: $I_{SnTe} : I_{CTS} : I_{SRC} = 7.1206 : 1.0607 : 1$.

Using these values in Equation 4, the resulting quantum efficiency (η) ratios are: $\eta_{SnTe} : \eta_{CTS} : \eta_{SRC} = 8.535 : 1 : 2.1731$.

These results indicate that MWCNT has a higher carrier concentration than RGO, which explains why CTS exhibits the highest photogeneration rate (G). However, the increased carrier concentration in CTS also leads to the passivation of radiative recombination pathways and enhancement of non-radiative processes, resulting in the lowest quantum efficiency (η) among the samples.

The observed red and blue shifts in the PL peaks of SnTe after incorporating MWCNT and RGO are attributed to changes in defect and impurity states within the SnTe matrix.

Calculation of Magneto-elastic energy:

According to magneto-elastic theory, the general strain tensor is coupled with the magnetization direction via the magneto-elastic energy, which activates all components of the RKKY interaction[7] in the presence of spin–orbit coupling (SOC)[4,5,7.8], serving as a source of magnetic anisotropy. The anisotropic magneto-elastic strain energy is given by the relation

$$E_{ME} = \sum_{i,j=x,y,z} \left(B_{ij}\xi_{ij}\alpha_i\alpha_j\right) \qquad \ldots\ldots\ldots\ldots\ldots (7)$$

Where $\xi_{i,j}$= component of the strain tensor, α_i= direction cosine of the strain tensor, and $B_{i,j}$ = magneto-elastic coupling coefficient.

Now, for the cubic crystal SnTe, the anisotropic magneto-elastic energy[4,5] is represented in Voigt notation as:

$$E_{ME}= B_1(\xi_{xx}\alpha_x^2+ \xi_{yy}\alpha_y^2+ \xi_{zz}\alpha_z^2) + 2B_2(\xi_{xy}\alpha_x\alpha_y + \xi_{yz}\alpha_y\alpha_z + \xi_{zx}\alpha_z\alpha_x) \qquad \ldots\ldots\ldots\ldots\ldots (8)$$

The anisotropic strain tensor of CNT@SnTe in Kbar is $= \begin{vmatrix} 110.37 & 38.11 & -12.79 \\ 38.11 & 24.02 & -3.50 \\ -12.79 & -3.5 & -898.08 \end{vmatrix}$

The corresponding component of magnetic moment is (-0.01 0.09 0.74) μ_B. By using equation (8), the calculated anisotropic magneto-elastic energy is -2.85 eV/cell.

Similarly, the anisotropic stress tensor of Gr@SnTe in Kbar is $= \begin{vmatrix} 704.07 & 113.59 & 50.86 \\ 113.59 & 639.90 & 3.42 \\ 50.86 & 3.42 & 6.92 \end{vmatrix}$

and the corresponding component of the magnetic moment is (0.04 0.03 0.01) μ_B. By using equation (8), the calculated anisotropic magneto-elastic energy is 1.169 eV/cell.

The anisotropic stress tensor of GRDO@SnTe in Kbar is $= \begin{vmatrix} 1299.7 & -209.68 & 93.887 \\ -209.68 & -1181.25 & -6.313 \\ 93.887 & -6.313 & 12.774 \end{vmatrix}$

and the corresponding component of the magnetic moment is (0.07 -0.02 0.02) μ_B. By using equation (8), the calculated anisotropic magneto-elastic energy is 3.91436 eV/cell.

Estimation of impurity and defect concentration:

We estimate the impurity and defect concentration from XRD, EDAX, XPS, and Raman spectroscopy and correlate them with HRTEM images.

XRD:- We estimate the approximate impurity percentage by calculating the area under the curve of all peaks of SnTe, and the corresponding impurity peaks of SnO_2, TeO_2, and Te of SnTe, CTS, and SRC. The ratio of the area under the curve of all peaks to the total individual impurity peaks gives the approximate percentage of impurity concentration. We compare this result with the multiphase Rietveld refinement of all of the synthesized samples with an impurity phase. This gives a clear estimation of defect concentration of the impurity phase, which is depicted in Table S VII.

TABLE S VII Estimation of impurity concentration from peak area ratio and Rietveld refinement.

Sample Name	Area ratio of all the peaks of SnO_2 to all of the peaks within the sample.	Approximate percentage of SnO_2		Area ratio of all the peaks of TeO_2 to all of the peaks within the sample.	Approximate percentage of TeO_2		Area ratio of all the peaks of Te to all of the peaks within the sample.	Approximate percentage of Te		Approximate impurity percentage (D_i)	
		From peak area ratio	From Rietveld refine-ment		From peak area ratio	From Rietveld refine-ment		From peak area ratio	From Rietveld refine-ment	From peak area ratio	From Rietveld refine-ment
SnTe	29.353	3.29	3.54	23.497	4.09	3.89	29.35	3.29	2.04	10.6	9.47
CTS	47.891	2.04	1.84	53.044	1.85	1.52	16.43	5.73	6.03	9.62	9.39

SRC	35.55	2.73	2.61	31.11	3.11	3.22	37.84	2.57	2.19	8.42	8.02

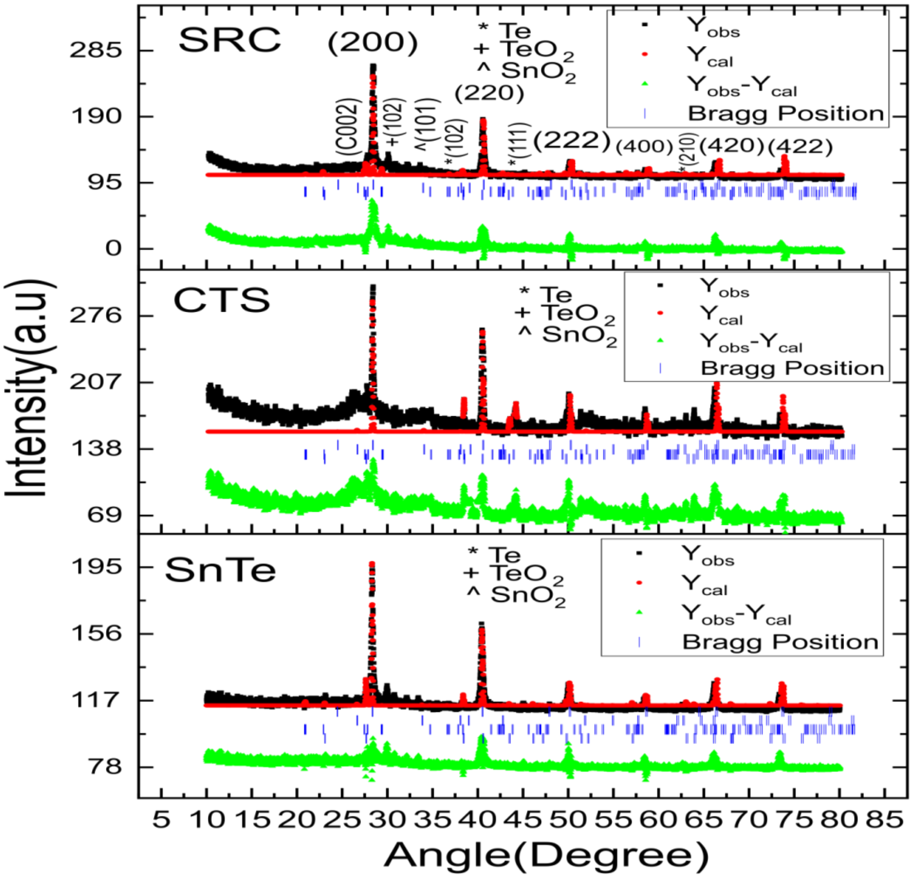

FIG. S4 Rietveld refinement of SnTe, CTS, and SRC using FullProf Software.

EDAX:- EDAX results of all synthesized compositions are shown in Table 1. For ideal SnTe, the approximate percentage of Sn and Te will be the same. The deviation of the Sn and Te percentage from the ideal value (i.e, close to 50%) arises due to impurity phases (such as SnO_2, TeO_2, and Te) and defect concentration. So, this percentage of deviation gives the approximate estimation of the impurity phase and defect concentration. Table S VIII depicts the approximate estimation of impurity and defect concentration. The deviation from the impurity and defect concentration gives the approximate percentage of defect concentration within the composite. The approximate defect percentage of SRC is higher than that of CTS, due to additional defects lying on the surface of RGO, which is consistent with the Raman results.

TABLE S VIII Estimation of impurity and defect concentration from EDAX result.

Sample Name	Atomic % of Sn (D_{Sn})	Atomic % of Te (D_{Te})	Atomic % of C	D_{Sn}-D_{Te}	Approximate impurity and defect percentage (D_{di})	Approximate total defect percentage $D_d = D_{di}-D_i$
SnTe	44.85	36.35	18.80	8.5	10.47	1

CTS	40.72	31.65	27.63	9.07	12.73	3.34
SRC	41.25	32.52	26.23	8.73	11.83	3.81

XPS:- X-ray photoelectron spectroscopy (XPS) reveals the surface impurity concentration of SnTe nano-grains, CTS, and SRC. The ratio of Sn^{2+} to Sn^{4+} and Te^{2-} to Te^{4+} oxidation states provides an estimate of surface impurity (SnO_2 and TeO_2) concentration, as detailed in Table S IX. From XRD peak area analysis and Rietveld refinement, the bulk impurity concentration (SnO_2 and TeO_2) within the SnTe nano-grains is approximately 9.47–10.6%, while XPS indicates a much higher surface concentration of ~40.65%. This discrepancy arises because XPS has higher surface sensitivity and resolution (5-10 nm depth of the sample) than XRD. Additionally, higher tendency of surface degradation[9], surface attachment of SnTe nano-grain on MWCNT and RGO via oxygen functional group, and higher defect densities on the surface of the nanoparticle due to defect migration from the core to the surface[6] for thermodynamic stability, contribute to this variation.

Assuming that impurities exist only on the surface of the synthesized composites, the impurity concentration derived from XRD can be used to estimate the surface-to-volume ratio. If the nanoparticles are approximated as circular discs with radius r and height h, this ratio can be used to calculate the nanoparticle thickness (h), as shown in Table S XI. The surface contribution is multiplied by 2, since XPS probes only one side of the disc-like particles.

The increased ratio of radius to height after the incorporation of MWCNT and RGO indicates an increase in effective surface area, leading to enhanced surface oxidation and topological surface state (TSS) conductivity. High-resolution TEM (HRTEM) images show that the diameters of the SnTe nano-grains range from 5 to 20 nm. So, the corresponding height of the NPs is in the order of 5.52 to 22.09 nm. ($l^2=r^2+h^2$)

TABLE S IX Estimation of surface impurity concentration from XPS result.

Sample Name	Area ratio of $Sn^{+2}/Sn^{+4}\_3d_{5/2}$	Area ratio of $Te^{-2}/Te^{+4}\_3d_{5/2}$	SnO_2:TeO_2:SnTe	Approximate impurity percentage on the surface (D_s)	Surface to volume ratio	Ratio of radii to lateral height of NPs (r/l)
SnTe	1.9778	0.4545	1:1.98:4.35	40.65%	51.9:48.1=1.079	1.8535/h
CTS	1.7724	0.2364	1:1.77:7.497	26.98%	41.88:58.12=0.7205	2.7758/h
SRC	1.8955	0.5	1:1.8955:3.7891	43.316%	36.5:63.5=0.5748	3.4794/h

We estimate the impurity and defect concentration on the surface of MWCNT and RGO from XPS C 1s spectra[2]. The area under the curve of C=C, C-C, and C=O peaks determines the approximate defect concentration on the surface of MWCNT and RGO. The percentage of the peak area of C=O gives the approximate percentage of defect concentration on the surface of MWCNT and RGO, which are depicted in Table S X. The deviation from the approximate total defect percentage (D_d) to defect percentage of C within MWCNT and RGO gives the defect percentage of Sn within the SnTe nano-grains, which are depicted in Table S X.

TABLE S X Estimation of surface impurity concentration of RGO and MWCNT from XPS result.

Sample Name	Area of C 1s C=C peak	Area of C 1s C-C and C-Sn peak	Area of C 1s C-Te peak	Area of C 1s C=O peak	Approximate defect percentage within MWCNT/ RGO (ρ_d)	Approximate defect percentage within composite ($\Omega_d=\rho_d*5\%$)	Approximate defect percentage of Sn within the SnTe nano-grains (D_d - Ω_d)
CTS	6939.44	3677.086	4228.23	4506.52	23.28	1.164	2.176
SRC	7285.83	2840.424	3568.3	4659.63	25.387	1.269	2.54

Raman:- Raman scattering is used to estimate the disorder in MWCNT and RGO[1]. The intensity ratio of D to G band (I_D/I_G) is directly proportional to the disorder. The evolution of disorder is estimated using the Tuinstra-Koenig relation1,2 LD C(λ) (ID/IG)-1, where LD is the average distance between defects in nm, and C(λ) is a proportionality constant of 4.4 nm. The approximate defect density per Cm^2 is given by the relation $n_D=10^{14}/\pi L_D^2$, which is depicted in Table S XI. A larger L_D value reveals better crystallinity within the system. The larger L_D value of CTS is the signature of fewer defects within it, which is consistent with XPS results.

TABLE S XI Estimation of defect density in CTS and SRC from Tuinstra-Koenig relation.

Sample Name	I_D/I_G	L_D	n_D in Cm^2
CTS	0.9682	4.5445	$1.5412\text{x}10^{12}$
SRC	1.2669	3.47307	$2.6389\text{x}10^{12}$

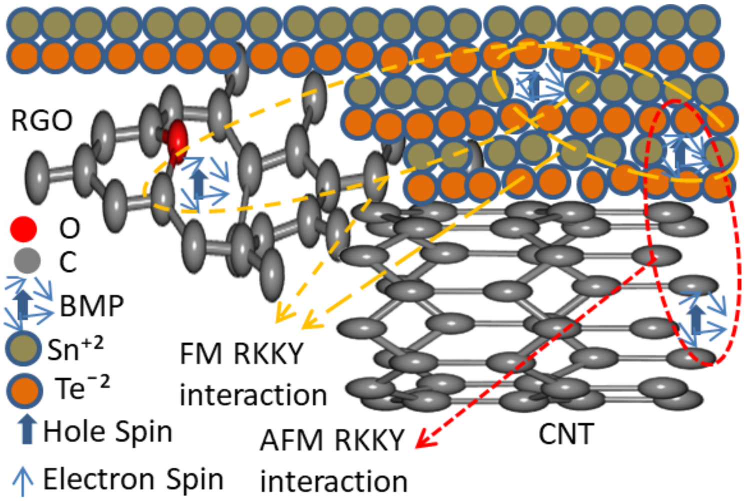

FIG S5 Schematic of magnetic interaction in SRC.

TABLE S XII The integrated charge content of C 2p orbital within the valence band up to -5 eV of Gr-2l-$_{\text{C182p}}$, Gr-2l@SnTe-$_{\text{C182p}}$, Gr-1l-$_{\text{C112p}}$, Gr-1l@SnTe-$_{\text{C112p}}$, CNT-S-$_{\text{C112p}}$, CNT-S@SnTe-$_{\text{C112p}}$, CNT-m-$_{\text{C112p}}$, CNT-m@SnTe-$_{\text{C112p}}$, GRD-1l-$_{\text{C122p}}$, GRD-1l@SnTe-$_{\text{C122p.}}$

Composition Symbol	Charge (a.u)
Gr-2l-C_{182p}	1.94578
Gr-2l@SnTe-$C_{18\text{-}2p}$	0.961546
Gr-1l-$C_{11\text{-}2p}$	1.186
Gr-1l@SnTe-$C_{11\text{-}2p}$	1.06591
CNT-S-$C_{11\text{-}2p}$	1.16753
CNT-S@SnTe-$C_{11\text{-}2p}$	1.01173
CNT-m-$C_{11\text{-}2p}$	1.16753
CNT-m@SnTe-$C_{11\text{-}2p}$	0.859265
GRD-1l-$C_{12\text{-}2p}$	0.455839
GRD-1l@SnTe-$_{\text{C12-2p}}$	0.73087

TABLE S XIII The integrated charge content of O 2p orbital within the valence band up to -5 eV of GRD-1l-$O_{11\text{-}2p}$, and GRD-1l@SnTe-$O_{11\text{-}2p}$.

Composition Symbol	Charge (a.u)
GRD-1l-$O_{11\text{-}2p}$	0.620901
GRD-1l@SnTe-$O_{11\text{-}2p}$	1.38027

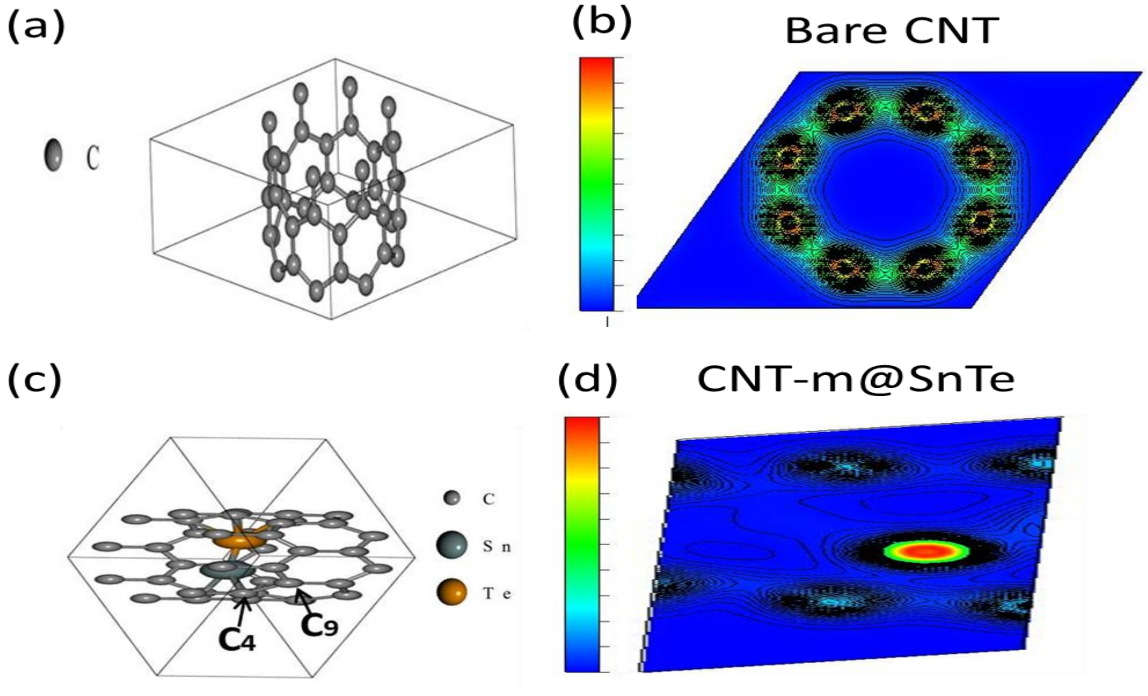

FIG S6 (a) Zigzag (0,8) CNT with 32 C atoms, (b) 2D electron density contour map of bare CNT, (c) Zigzag (0,8) CNT with adsorbed SnTe at the center (CNT-m@SnTe), (d) 2D electron density map of SnTe adsorbed CNT (CNT@SnTe).

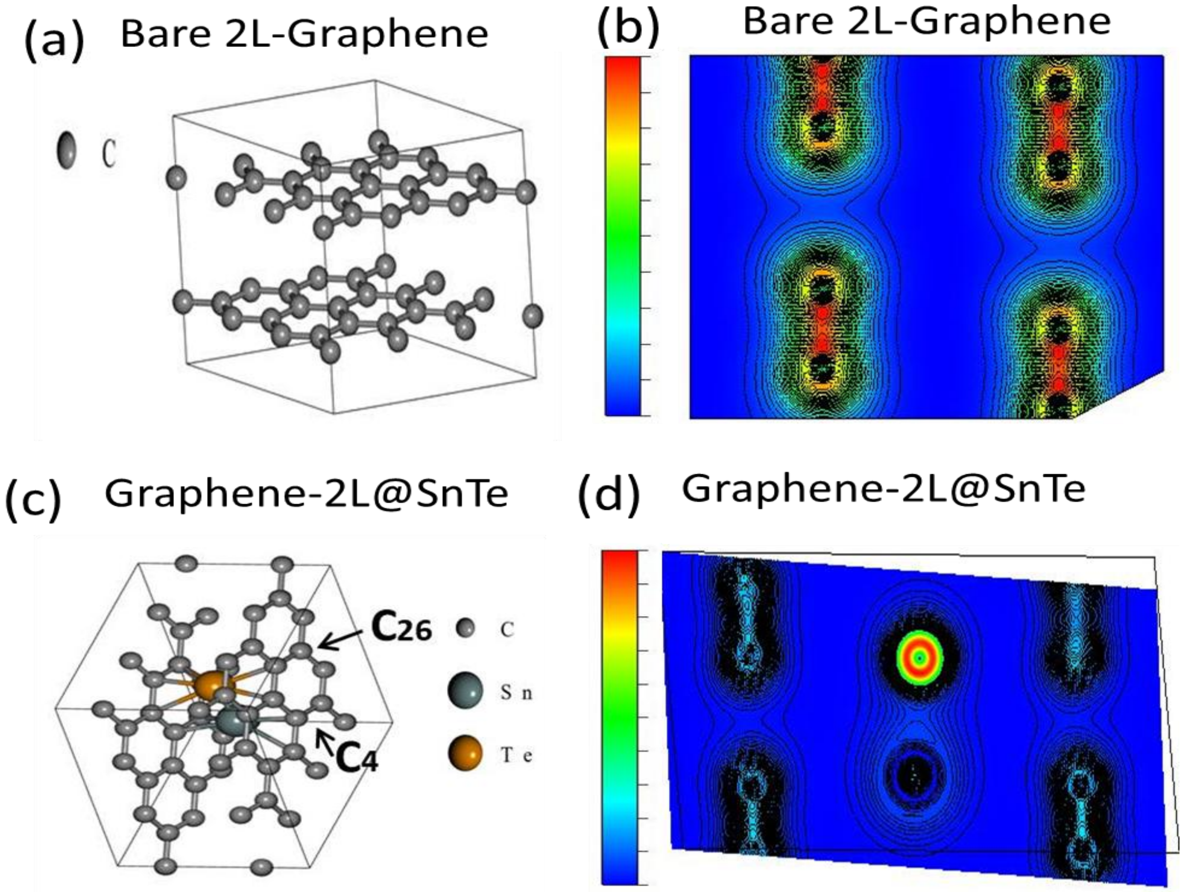

FIG S7. (a) Two layers of graphene (2L) with 36 C atoms (b) 2D electron density map of two-layer bare graphene (2L) (c) SnTe adsorbed two layers of graphene (2L) with 36 C atoms (Gr-2l-@SnTe) (d) 2D electron density map of Gr-2l@SnTe.

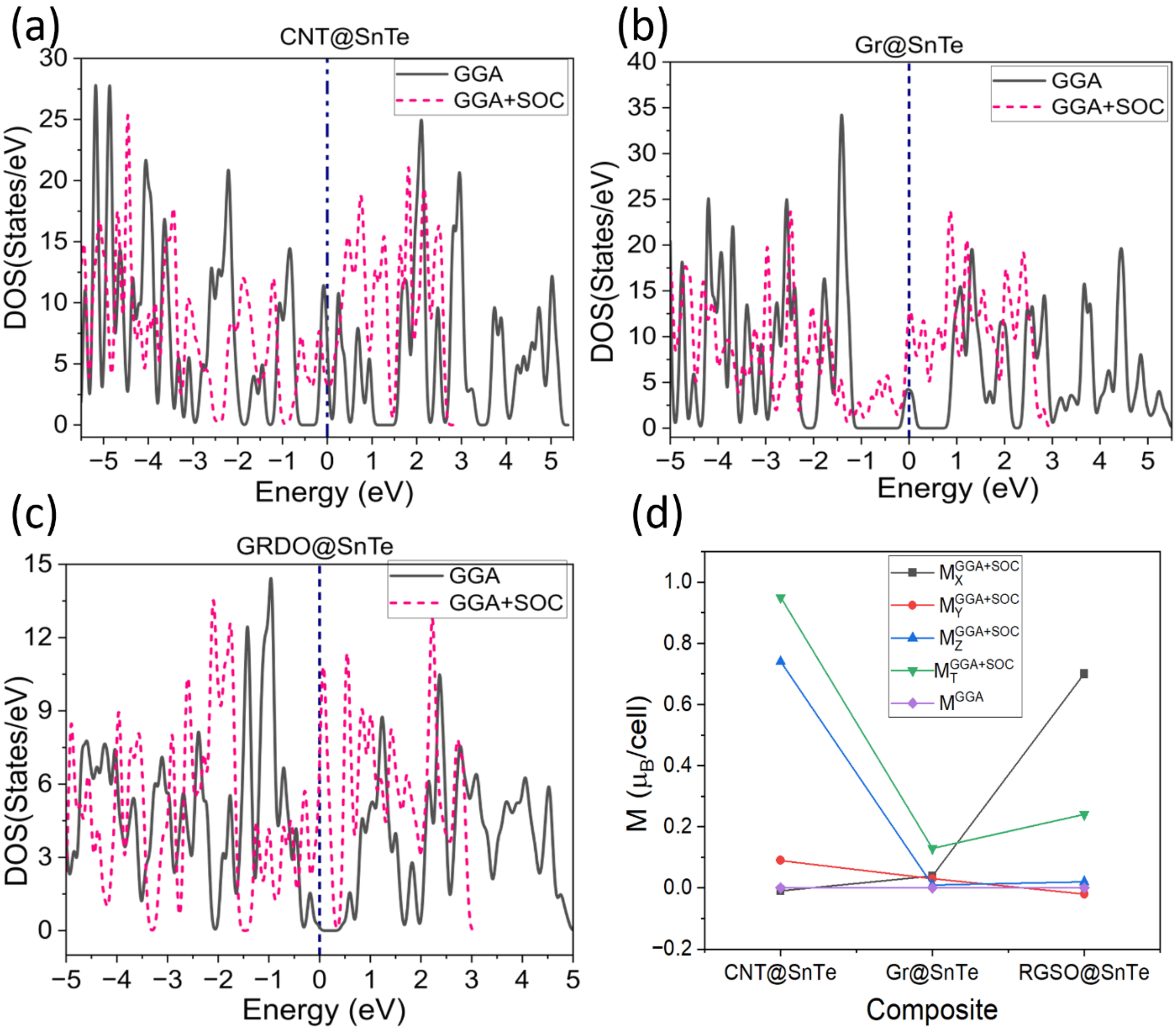

FIG. S8. DOS of (a) CNT@SnTe, (b) Gr@SnTe, and (c) GRDO@SnTe with GGA and noncollinear GAA+SOC calculation. (d) Different components of the magnetic moment with GGA and noncollinear GAA+SOC calculation.

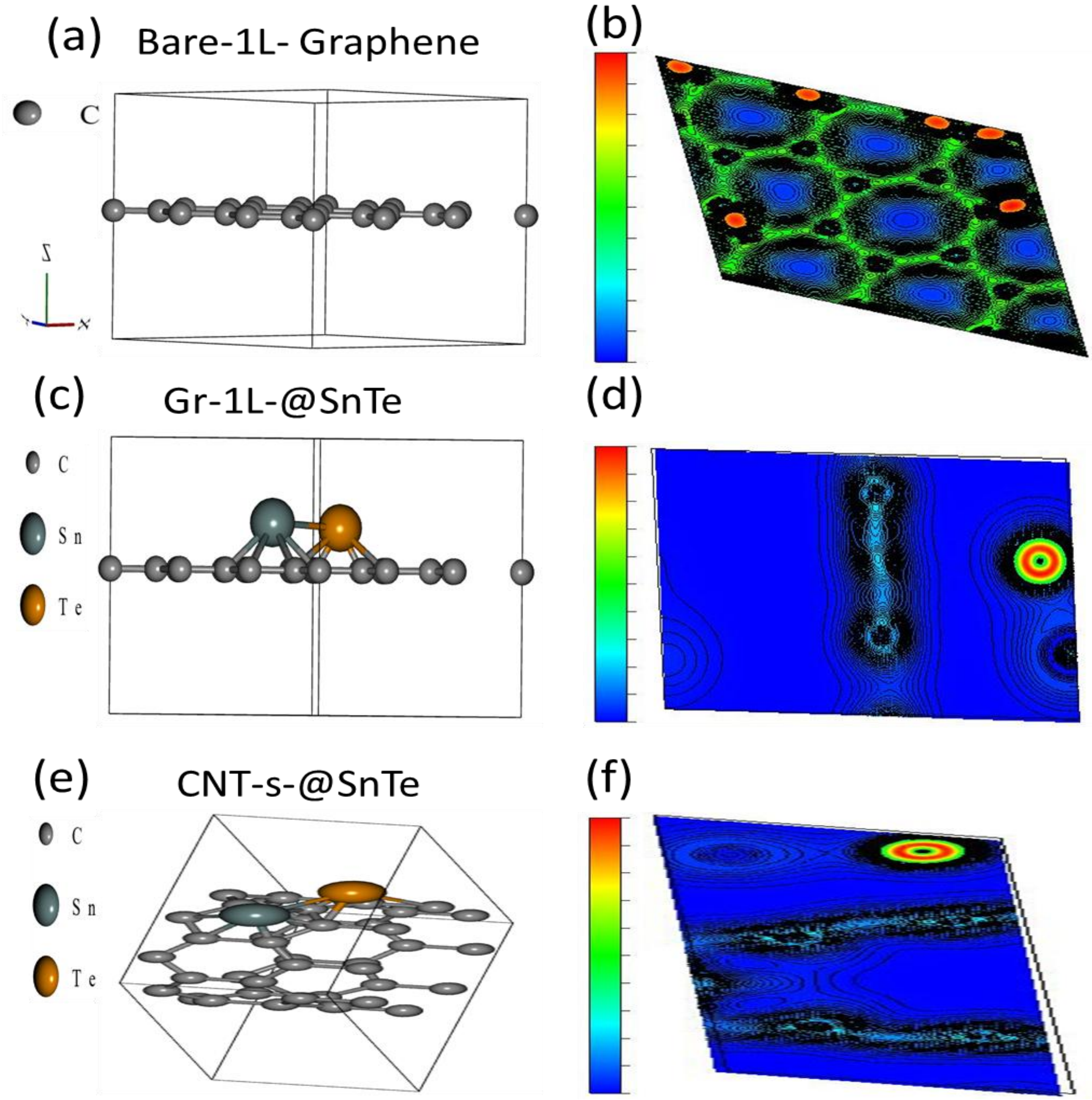

FIG S9. (a) Single layer of Graphene with 18 C atoms (b) The contour 2D charge density plot of single layer of Graphene, (c) SnTe adsorbed single layer graphene (Gr-1L-@SnTe) (d) 2D electron density map of Gr-1L@SnTe (e) SnTe adsorbed CNT on the surface (CNT-s-@SnTe) and (f) 2D electron density map of SnTe adsorbed CNT on the surface (CNT-s-@SnTe).

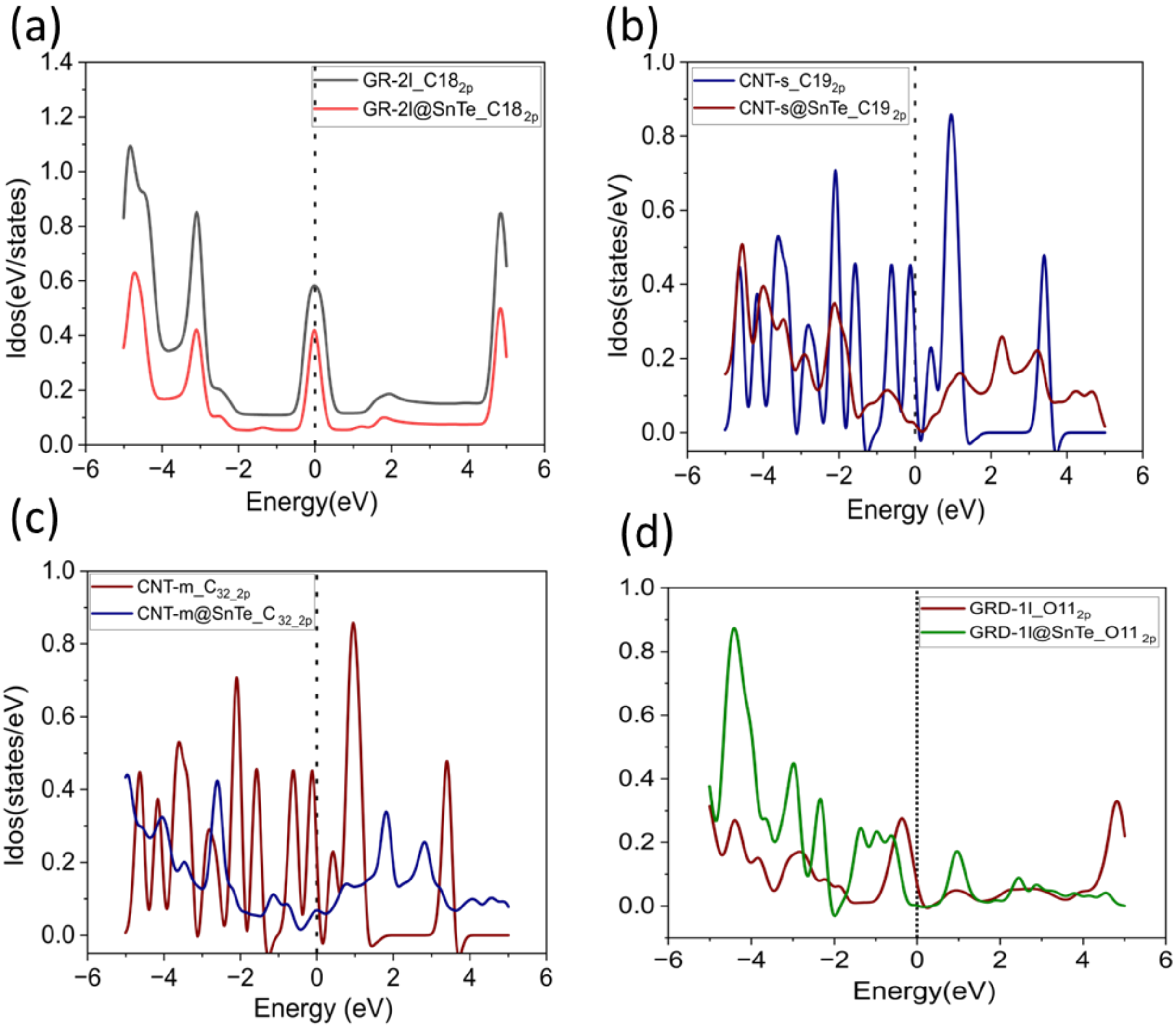

FIG. S10. Comparison of the local density of states of C 2p orbital of (a) double-layers of graphene and SnTe adsorbed graphene (Gr-2l@SnTe), (b) bare CNT and SnTe adsorbed CNT on its surface, (c) bare CNT and SnTe adsorbed CNT at its center, and (d) Comparison of the local density of states of O 2p orbital of GRDO-1l-O$_{11-2p}$, and GRDO-1l-O$_{11-2p}$.

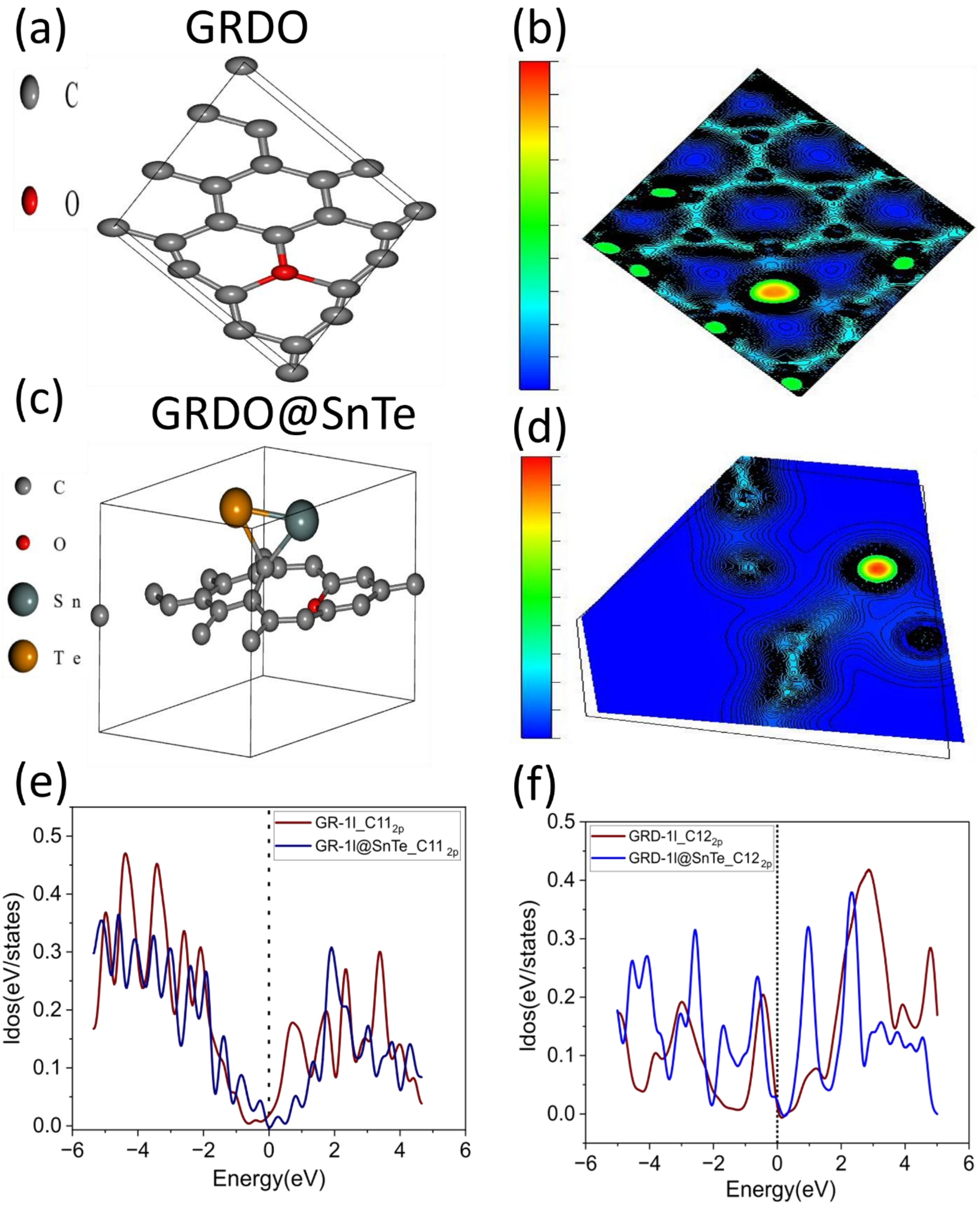

FIG. S11. (a) Graphene with one C vacancy and one Oxygen atom (GRDO), (b) 2D electron density map of GRDO, (c) GRDO with adsorbed SnTe (GRDO@SnTe), (d) 2D electron density map of GRDO@SnTe, (e) Comparison of the local density of states of C 2p orbital of GRDO$_{1l}$C11$_{2p}$, and GRDO$_{1l}$@SnTe-C11$_{2p}$, and (f) Single layer graphene and SnTe adsorbed graphene (Gr$_{1l}$@SnTe).

Calculation of strain from XRD:

According to the Uniform Stress Deformation Model, stress acts in all directions of the lattice planes uniformly as a result of uniform deformation. According to Hooke's law, stress (σ) and strain (ε) are related to Young's modulus (Y) via the relation:

$$\sigma = Y.\ \varepsilon$$

Now we can estimate the strain from the deformation of the lattice parameter via the relation:

$$\varepsilon = \frac{a - a0}{a0}$$

Where a_0 is the lattice parameter of the unstrained or pristine sample, and a is the lattice parameter of the sample with strain. Here, we consider the lattice parameter of pristine SnTe as a_0, and the lattice parameter of CTS and SRC as a. The strain and the corresponding stress of CTS and SRC are shown in Table S XIV. (Here we use the Young's modulus of SnTe as 55.6 GPa.)

TABLE S XIV

Sample Name	Lattice Parameter	Strain	Stress in GPa	Stress in Kbar
SnTe	6.305	0	0	0
CTS	6.335	0.004758	0.2645	2.645
SRC	6.3266	0.00342585	0.190477	1.9047

Thermogravimetric Study

The TG curves for SnTe, CTS, and SRC were recorded at a heating rate of 10 K/min over the temperature range of 40 °C to 900 °C under an inert nitrogen (N_2) atmosphere to prevent atmospheric degradation[10,11]. Figure S12(a) displays the TG curves of the three samples, each exhibiting four distinct decomposition steps[10–12]. In the temperature range of 50 °C to 254 °C, the SRC shows the highest decomposition rate, while SnTe exhibits the lowest. This enhanced decomposition in SRC is attributed to the breakdown of van der Waals interactions between SnTe nanoparticles and the surfaces of reduced graphene oxide (RGO) and multi-walled carbon nanotubes (MWCNTs). Due to RGO's planar structure, SRC contains a higher number of van der Waals interactions, resulting in greater mass loss in this low-temperature range (40 ^{0}C-254 ^{0}C). Beyond 254 °C, SnTe undergoes a gradual mass loss up to 672 °C. After 672 °C, a slight mass gain is observed, followed by a sharp mass loss beyond 756 °C, which corresponds to the decomposition of Sn–Te bonds[11,12].

The CTS composite exhibits a somewhat different decomposition profile: A minor mass gain occurs between 515 °C and 592 °C, followed by a sharp mass loss from 592 °C to 646 °C. A significant mass increase is then observed between 646 °C and 756 °C, before a final sharp decomposition beyond 756 °C, also linked to Sn–Te bond breakage.

SRC shows a similar decomposition pattern to CTS, with a key difference that it exhibits a more pronounced mass increase from 425 °C to 592 °C. This is due to additional endothermic and exothermic reactions between RGO/MWCNTs and N_2, facilitated by various surface functional groups and defect states[12].

Notably, SRC experiences larger mass changes than CTS in the 425 °C to 756 °C range, primarily due to the greater number of defects and oxygen-containing functional groups in RGO compared to MWCNTs.

Figure S12(b) and Table S XV summarize the total decomposition percentages. All samples show similar overall mass loss, likely due to decomposition of carbonaceous contaminants introduced by ethanol used during sample preparation. CTS exhibits slightly higher decomposition (by 0.27%) compared to SnTe, attributed to the breakdown of oxide functional groups in MWCNTs[10–12].

SRC shows the highest total decomposition (18.54%), due to its greater content of defects and oxygen-containing groups in RGO relative to MWCNT [10–12].

TABLE S XV Observation of total mass loss in Percentage of SnTe, CTS, and SRC.

Sample	**Heating rate (K.min^{-1})**	**Total mass loss in %**
SnTe NPs	10	17.55
CTS	10	17.82
SRC	10	18.54

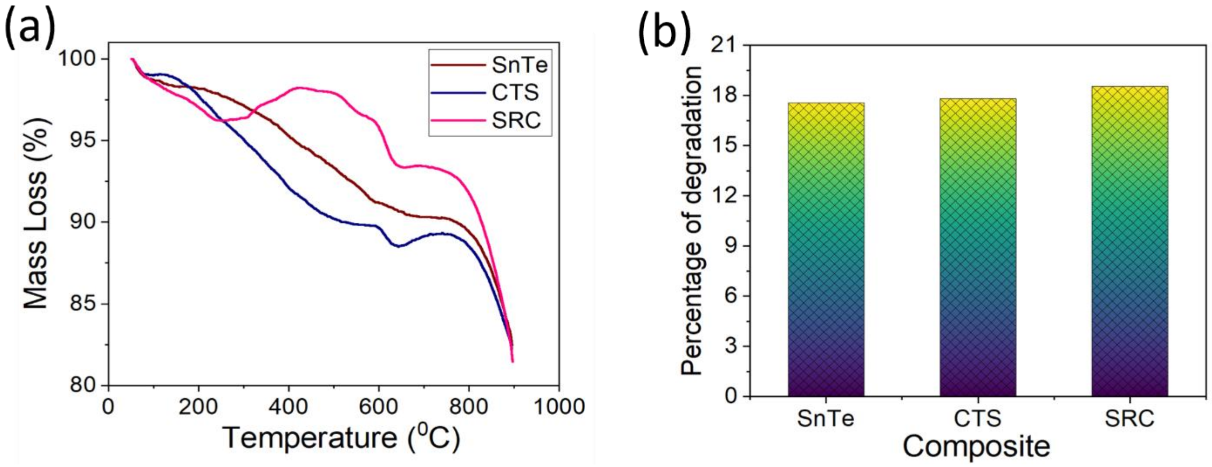

FIG. S12. (a) TG curves of SnTe, CTS, and SRC, (b) 2D electron density map of GRDO.

Reference:

[1] M.M. Lucchese, F. Stavale, E.H. Martins Ferreira, C. Vilani, M.V.O. Moutinho, Rodrigo B. Capaz, C.A. Achete, A. Jorio, Quantifying ion-induced defects and Raman relaxation length in graphene, Carbon, 5, 1592—1597 (2010).
[2] K. Ganesan, Subrata Ghosh, Nanda Gopala Krishn, S. Ilango, M. Kamruddinab and A. K. Tyagi, A comparative study on defect estimation using XPS and Raman spectroscopy in few-layer nanographitic structures, Physical Chemistry Chemical Physics, 18, 32, 22160—22167(2016).
[3] H. Phirke;; S. Gharabeiki ; A. Singh, A. Krishna ; S. Siebentritt ; A. Redinger, Quantifying recombination and charge carrier extraction in halide perovskites via hyperspectral time-resolved photoluminescence imaging, APL Energy, 2, 01, 6111 (2024).
[4] B. D. Hoi, Physical Review B, 2024, 109, 184441.
[5] W. D. Armstrong, Journal of Magnetism and Magnetic Materials, 2003, 263, 208–218
[6] G. C. Papaefthymiou, Nano Today, 2009, 4, 438–447.
[7] Mohsen Yarmohammadi, Hosein Cheraghchi, Effective low-energy RKKY interaction in doped topological crystalline insulators, PHYSICAL REVIEW B **102**, 075411 (2020).
[8] Anna Ciechan, Piotr Bogusławski, Theory of the *sp–d* coupling of transition metal impurities with free carriers in ZnO, Scientific Reports, **11**,1,3848,(2021).
[9] N. Berchenko, R. Vitchev, M. Trzyna, R. Wojnarowska-Nowak, A. Szczerbakow, A. Badyla, J. Cebulski and T. Story, Applied Surface Science, 2018, 452, 134–140.

[10] Kannaujiya, M Rohitkumar and Chaki, H Sunil and Khimani, J Ankurkumar and Parekh, R Zubin and MP Deshpande, Kinetic stability of tin telluride nanoparticles synthesized by hydrothermal method, Chemical Thermodynamics and Thermal Analysis, **6**, 100058 (2022).
[11] Kannaujiya, M Rohitkumar and Chaki, Sunil H and Khimani, J Ankurkumar and Hirpara, B Anilkumar and Parekh, R Zubin and Giri, Ranjan Kr and Patel, Shivam and MP Deshpande, Journal of Materials Science: Materials in Electronics, **33**, 26, 20823-20836 (2022).
[12] Han, Guang and Zhang, Ruizhi and Popuri, Srinivas R and Greer, Heather F and Reece, J Michael and Bos, G Jan-Willem and Zhou, Wuzong and Knox, R Andrew and Gregory, H Duncan, Large-scale surfactant-free synthesis of p-type SnTe nanoparticles for thermoelectric applications, **10**, 3, 233 (2017).
[13] Kunjal Patel, Anand Patel, Vibhutiba P Jethwa, Hetal Patel, and GK Solanki, X-ray diffraction analysis of orthorhombic SnSe nanoparticles by Williamson--Hall, Halder--Wagner and Size--Strain plot methods, Chemical Physics Impact, 8, 100547 (2024).